J Mater Sci: Mater Electron (2026) 37:1250

CuO-integrated WS_2 electrodes on stainless steel for efficient energy storage applications

H. E. Kırtay[1], S. R. Tokgöz[1], and A. Peksöz[1,*]

[1] *Physics Department, Faculty of Arts and Sciences, Bursa Uludağ University, Görükle Campus, 16059 Bursa, Turkey*

Received: 26 January 2026
Accepted: 15 May 2026

© The Author(s), 2026

ABSTRACT

This study presents a unique hierarchical architecture in which the synergistic effect between the high-capacity CuO framework and conductive WS_2 nanosheets is effectively utilized. In contrast to traditional electrode systems, the binder-free heterostructure directly grown on the stainless steel substrate offers faster ion-transport channels and improved mechanical stability during repeated redox reactions. XRD and Raman spectroscopy analyses verify the successful formation of the desired molecular phases. Electrochemical measurements performed in a 1 M LiCl electrolyte with a three-electrode system reveal enhanced charge-storage performance for the hybrid structure. Notably, the CuO@WS_2/SS electrode delivers a specific capacitance of 665 F g^{-1} at 10 mV s^{-1}, which is substantially higher than that of pristine WS_2/SS (385 F g^{-1}). Kinetic analysis based on the power-law relationship indicates that charge storage in the CuO@WS_2/SS composite electrode arises from both diffusion-driven and surface-controlled mechanisms. The incorporation of CuO markedly increases the capacitive contribution, reaching 66% at 70 mV s^{-1} and 80% at 300 mV s^{-1}, compared with the pristine WS_2/SS electrode. To evaluate practical applicability, a symmetric supercapacitor (SSC) device is assembled by using the CuO@WS_2/SS electrodes with a 1 M LiCl aqueous electrolyte. The device exhibits an impressive operating potential window of 1.5 V and demonstrates exceptional long-term stability with 94.6% capacitance retention after 10,000 continuous charge–discharge cycles. Furthermore, the SSC device delivers a maximum energy density of 30.8 Wh kg^{-1} at a power density of 1155 W kg^{-1} (at a specific current of 1 A g^{-1}). Even at a high power density of 4696 W kg^{-1} (at 5 A g^{-1}), it maintains a significant energy density of 9.3 Wh kg^{-1}. These results highlight the potential of transition metal chalcogenide/oxide heterostructures for high-performance and durable energy storage solutions.

Address correspondence to E-mail: peksoz@uludag.edu.tr

https://doi.org/10.1007/s10854-026-17609-x
Published online: 04 June 2026

1 Introduction

The rapid growth of the global population leads to an increasing demand for electrical energy. Energy production and consumption predominantly rely on fossil fuels, despite their considerable impact on both the global economy and the environment. Alternatively, renewable energy sources are currently in high demand. In renewable energy systems, energy storage devices offer several advantages, including a wide operating temperature range, good cycling stability, low cost, fast charge–discharge capability, and high power density. Cycling stability is a key parameter in energy storage devices and significantly influences their operational lifetime [1]. Certain design improvements enable them to endure extended charge–discharge cycles. Owing to their unique combination of fast charge-transfer kinetics and strong structural stability, supercapacitors emerge as a key technology for modern energy demands. These devices bridge the gap between batteries and conventional capacitors by providing both high-rate performance and long operational life. Several approaches exist to enhance the performance of supercapacitors. These strategies include tailoring electrode morphology, improving chemical and structural stability, optimizing electrical conductivity, and incorporating advanced materials [2]. The key parameters that enhance the electrochemical performance of electrodes include high porosity, a large active surface area, good electrical conductivity, and abundant redox-active sites [3].

Metal oxides have recently attracted considerable attention as promising materials for high-performance supercapacitor electrodes due to their large surface area and excellent electrochemical properties. As supercapacitor materials, metal oxides are widely favored owing to their natural abundance, low cost, environmentally benign nature, and straightforward synthesis routes [2]. In particular, binary metal oxides exhibit excellent electrochemical performance due to their enhanced conductivity and rapid redox reactions during electrochemical processes [1]. The increased surface area in doped metal oxides enhances charge-storage capability in supercapacitor and battery systems by promoting electrochemical reactions. In addition, metal oxides exhibit excellent cycling stability with minimal performance degradation [4]. This feature makes them suitable for long-term applications. In addition, their porous structures facilitate efficient ion transport and charge storage, leading to high capacitance [5, 6]. Doped metal oxides further advance the performance of energy storage and conversion systems by simultaneously improving charge transport, structural robustness, catalytic activity, long-term cycling behavior, and accessible active surface [7–11]. Metal oxides play a significant role in next-generation energy systems due to their unique properties, enabling the development of advanced energy storage technologies.

The increasing use of metal sulfides in hybrid device fabrication is driven by their strong electrochemical activity [12]. In metal sulfides, sulfur's lower electronegativity compared to oxygen enhances capacitance and structural flexibility, while their high redox activity supports efficient electrochemical processes in batteries and supercapacitors. This property enables efficient participation in charge–discharge processes, thereby improving energy storage capacity. Transition and post-transition metal sulfides also exhibit high electrical conductivity, which facilitates effective electron transport during electrochemical operation. These characteristics are essential for achieving high power density in energy storage devices [13]. Moreover, metal sulfides are highly versatile materials with wide applicability in energy storage systems. Their structural adaptability enables integration into different architectures, including high-power supercapacitors and alkali-metal (Li, Na, and K) ion batteries [14]. Metal sulfide-based electrodes exhibit excellent cycling stability, retaining a significant portion of their initial capacitance over thousands of charge–discharge cycles. This property is crucial for energy storage systems that demand long-term durability [15]. Furthermore, they can be easily combined with materials such as carbon-based structures to form composites with improved electrochemical performance.

The primary motivation of this research is to address the inherent limitations of transition metal dichalcogenides (TMDCs), particularly the low electrical conductivity and sluggish surface kinetics of WS_2, which restrict their practical use in high-rate supercapacitors. Despite various enhancement strategies, achieving high-performance materials through controlled synthesis remains challenging and requires more advanced integration approaches. This study distinguishes itself from previous reports by integrating CuO nanostructures onto WS_2 nanosheets directly grown on stainless steel substrates, forming a binder-free hierarchical architecture. Unlike conventional composite

electrodes that depend on conductive additives, this work focuses on the quantitative deconvolution of charge-storage kinetics to elucidate how CuO modification alters the balance between diffusion-controlled and surface-controlled processes. By systematically analyzing capacitive contribution over a wide range of scan rates, this study reveals the interfacial synergy between CuO and WS_2 and provides a robust approach for designing high-performance electrodes with optimized pseudocapacitive behavior.

Transition metal dichalcogenides and metal oxides have been extensively studied for electrochemical energy storage applications; however, significant limitations still remain for practical implementation, particularly low electrical conductivity, restricted ion transport, and limited utilization of electroactive sites. In previously reported systems [16, 17], these limitations are generally linked to the use of single-component materials or binder-based powder electrodes, which can reduce charge-transfer efficiency and structural stability. In this context, a CuO–WS_2 hybrid architecture is developed directly on a conductive stainless steel substrate via an electrochemical approach, eliminating insulating binders and enhancing interfacial contact. The originality of this work lies in the design of a heterostructured electrode that enables synergistic interactions between CuO and WS_2, improving ion diffusion pathways and increasing the accessibility of active sites. Furthermore, the charge-storage mechanism is systematically evaluated, showing that both diffusion-controlled and surface-controlled processes contribute significantly to the overall capacitance. Compared to conventional WS_2-based electrodes, a substantial improvement in capacitive contribution, rate capability, and long-term cycling stability has been achieved. These findings indicate that the designed hybrid structure provides an effective strategy for optimizing pseudocapacitive behavior and offers a promising route for the development of high-performance energy storage systems. Compared to conventional WS_2-based electrodes, the hybrid structure delivers significantly improved capacitive contribution, rate capability, and long-term cycling stability. These results demonstrate that the designed architecture effectively enhances pseudocapacitive behavior and provides a promising strategy for developing high-performance energy storage systems.

2 Experimental

2.1 Materials

The chemical reagents, including sodium tungstate dihydrate ($Na_2WO_4{\cdot}2H_2O$, 99%), sodium thiosulfate ($Na_2S_2O_3{\cdot}5H_2O$, ≥ 98%), lithium chloride (LiCl, ≥ 99%), hydrochloric acid (HCl, 37%), copper sulfate pentahydrate ($CuSO_4{\cdot}5H_2O$, 98%), and hydrogen peroxide (H_2O_2, 35%), are purchased from Sigma-Aldrich Company (UK) and utilized without further purification. Stainless steel (SS) serves as the working electrode substrate. To ensure strong adhesion and a high-quality surface for electrodeposition, the SS substrates are subjected to a thorough mechanical and chemical cleaning procedure. Initially, the surfaces are polished using fine-grit sandpaper. This is followed by a sequential ultrasonic cleaning cycle lasting 75 min, involving immersion in ultrapure water, acetone, 2-propanol, and hydrochloric acid. Finally, the prepared substrates are dried under a steady stream of nitrogen gas to ensure a contaminant-free surface.

2.2 Synthesis of CuO@WS_2/SS electrodes

For the synthesis of the CuO layer, an aqueous precursor solution is prepared by dissolving 10 mM $CuSO_4{\cdot}5H_2O$ and 0.2 M LiCl in 50 mL of ultrapure water, and the pH is adjusted to the desired value using a few drops of HCl. The mixture is continuously stirred until a homogeneous solution is obtained. The metallic Cu precursor is subsequently deposited onto the stainless steel (SS) substrate via galvanostatic electrodeposition at a stabilized potential of − 0.4 V for 420 s. To induce phase transformation from metallic Cu to CuO, the deposited films are thermally annealed at 450 °C for 2 h in air.

To synthesize the WS_2 layer on the SS substrate, a secondary electrolyte bath is prepared by dissolving 20 mM $Na_2S_2O_3{\cdot}5H_2O$, 10 mM $Na_2WO_4{\cdot}2H_2O$, 0.2 M LiCl, and 0.05 M H_2O_2 in 50 mL of ultrapure water. The pH is adjusted to 2 using controlled additions of HCl. The co-electrodeposition of W and S species onto the SS substrate is then performed at a constant potential of − 0.8 V for 600 s. The proposed electrochemical formation mechanism of WS_2 on the stainless steel substrate can be explained as follows. The process involves the electrochemical reduction of tungstate ions (WO_4^{2-}) to lower-valence tungsten

species at the cathode surface, while thiosulfate ions ($S_2O_3^{2-}$) are simultaneously decomposed in the presence of H_2O_2 to generate reactive sulfur species (S^{x-}). The in situ generated sulfur species subsequently react with reduced tungsten ions, leading to nucleation and growth of WS_2 through an ion-by-ion deposition mechanism. The overall process is governed by coupled reduction–oxidation reactions and interfacial charge transfer, resulting in the formation of a uniform WS_2 layer on the substrate. After the deposition step, the WS_2/SS electrode is dried under ambient laboratory conditions. Subsequently, the WS_2 layer is deposited onto the previously prepared CuO/SS substrate using the same electrochemical parameters described above. The resulting CuO@WS_2/SS structure is then annealed at 450 °C for 1 h. Figure 1 schematically presents the synthesis route of the WS_2/SS and CuO@WS_2/SS electrodes. Accordingly, two electrode configurations—WS_2/SS and CuO@WS_2/SS—are fabricated for comparative performance evaluation.

2.3 Analytical techniques and electrochemical performance testing

Surface morphologies of the fabricated electrodes are examined using scanning electron microscopy (SEM) with a Carl Zeiss EVO 40 system (Carl Zeiss NTS Limited Company, Cambridge, UK). The crystalline nature and phase composition of the samples are determined via X-ray diffraction (XRD) analysis. Additionally, a Renishaw Raman Microscope is utilized to further investigate the surface phase characteristics and vibrational modes of the electrodes.

A conventional three-electrode configuration is used for all electrochemical measurements and controlled using a Gamry Reference 3000-E workstation. In this setup, the synthesized material on stainless steel serves as the working electrode, while a graphite rod and Ag/AgCl electrode act as the counter and reference electrodes, respectively. The 1 M LiCl aqueous electrolyte is selected as a neutral medium to minimize side reactions and structural degradation of the electrode, while providing sufficient ionic conductivity for reliable electrochemical evaluation.

3 Results and discussion

3.1 Surface analyses of the electrodes

The surface morphologies of the fabricated electrodes are presented in the SEM images shown in Fig. 2. The pristine WS_2/SS electrode (Fig. 2a) shows a relatively uniform and compact distribution of fine particles on the stainless steel substrate. In contrast, the CuO@WS_2/SS electrode (Fig. 2b) exhibits a clear morphological change, where spherical CuO nanoparticles are uniformly distributed on the WS_2

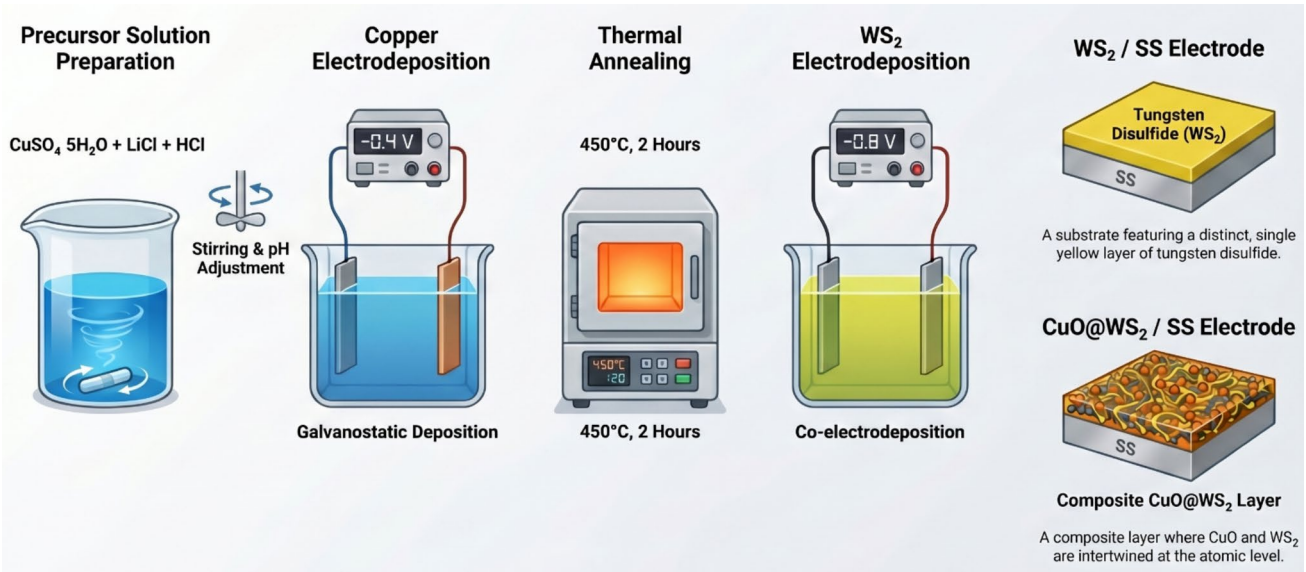


Fig. 1 Schematic illustration of the step-by-step fabrication process of the WS_2/SS and CuO@WS_2/SS electrodes, including electrodeposition and subsequent thermal annealing treatments

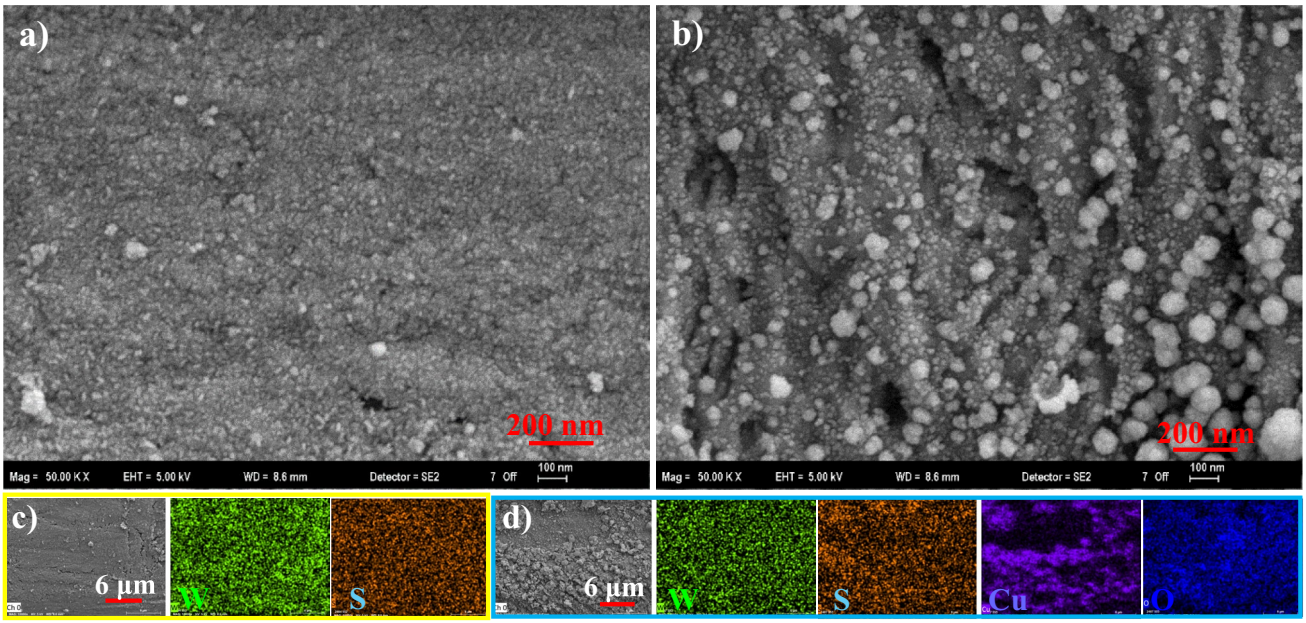


Fig. 2 Morphological and elemental characterization of the fabricated electrodes: **a** SEM micrograph of the pristine WS_2/SS electrode **b** SEM micrograph of the CuO@WS_2/SS composite electrode, **c** EDS elemental mapping of the WS_2/SS surface confirming the uniform distribution of W and S, and **d** EDS elemental mapping of the CuO@WS_2/SS composite validating the simultaneous presence and homogeneous dispersion of W, S, Cu, and O species

surface. These CuO clusters form a more hierarchical and porous surface structure, increasing the density of electroactive sites and enhancing ion transport at the electrode–electrolyte interface.

The elemental distribution and chemical homogeneity of the electrodes are further confirmed by EDS mapping analysis (Fig. 2c and d). For the WS_2/SS electrode (Fig. 2c), the maps verify the presence and uniform distribution of W and S, indicating the successful formation of a continuous WS_2 layer. In the CuO@WS_2/SS composite (Fig. 2d), the coexistence of W, S, Cu, and O signals confirms the effective incorporation of CuO within the WS_2 matrix. The overlapping elemental signals indicate a uniform dispersion of CuO nanoparticles throughout the WS_2 framework with minimal agglomeration. This intimate interfacial contact is essential for enhancing synergistic electrochemical interactions and improving charge-transfer kinetics in the hybrid electrode. The weight percentage of CuO in the CuO@WS_2 composite is calculated based on the mass ratio of the active materials. Accordingly, the CuO content in the CuO@WS_2/SS electrode is determined to be 29.2 wt%.

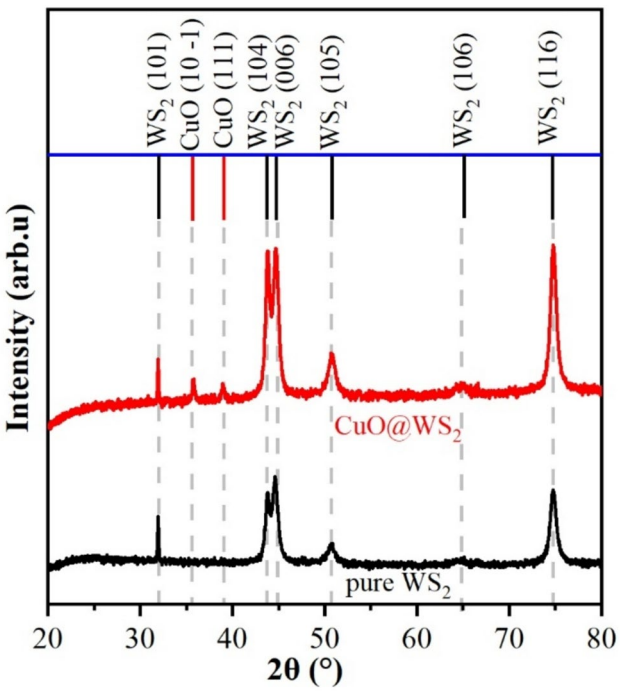


Fig. 3 XRD spectra of WS_2/SS and CuO@WS_2/SS

3.2 XRD and Raman studies

Figure 3 presents the XRD patterns of the synthesized materials. For pristine WS_2, the diffraction peaks observed at specific 2θ positions correspond to the characteristic planes of hexagonal WS_2, confirming good crystallinity and phase purity. In the CuO@WS_2 sample, the main WS_2 diffraction peaks remain clearly visible, indicating that the layered WS_2 structure is preserved after composite formation. For the both material, the XRD peaks at 31.9, 43.9, 44.6, 50.8, 61.1, and 74.8° correspond to (1 0 1), (1 0 4), (0 0 6), (1 0 5), (1 0 6), and (1 1 6) crystalline planes of WS_2, respectively (JCPDS No. 01-084-1398 and 08-0237) [16]. In the XRD pattern of the CuO@WS_2 composite, the additional peaks observed at 35.8 and 38.4° are, respectively, assigned to the (1 1 − 1) and (1 1 1) crystallographic planes of the CuO phase (PDF# 48-1548) [17, 18].

The Raman spectra provide clear evidence of the structural characteristics of pristine WS_2 and the CuO@WS_2 composite. For the WS_2 material, two distinct peaks are observed at approximately 351 and 420 cm^{-1} (Fig. 4). These bands correspond to the characteristic in-plane (E^1_{2g}) and out-of-plane (A_{1g}) vibrational modes of layered WS_2, confirming the preservation of its hexagonal crystal structure [19]. In the Raman spectrum of CuO@WS_2, the WS_2-related modes are still present, indicating that the WS_2 framework remains preserved after CuO incorporation. In addition to these modes, new bands appear at around 209 and 274 cm^{-1} due to the vibrational modes of CuO [20]. These additional peaks verify the successful deposition of CuO on the WS_2 surface. Moreover, slight changes in the intensity and shape of the WS_2 modes in the composite indicate an interaction between CuO and WS_2. Thus, the combined spectroscopic and crystallographic results confirm the successful formation of a unified CuO@WS_2 framework, demonstrating that the designed hybrid morphology is effectively achieved.

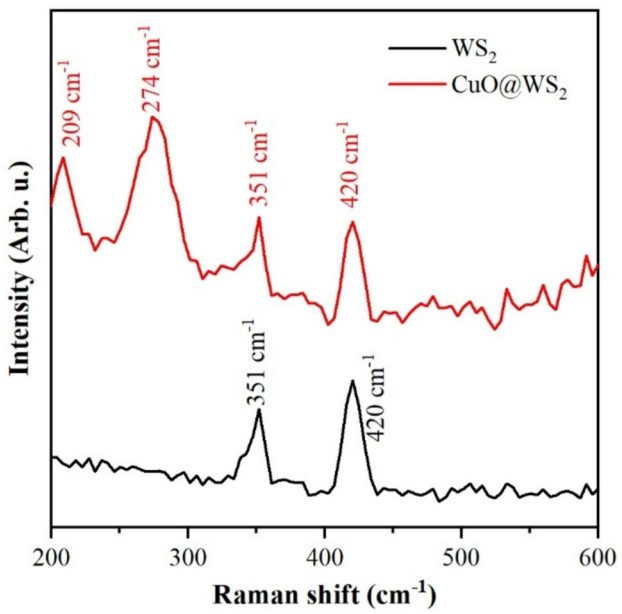


Fig. 4 Raman spectra of WS_2/SS and CuO@WS_2/SS

The convergence of these crystallographic and spectroscopic results confirms that the CuO@WS_2 heterostructure is formed with high phase purity, maintaining the intrinsic properties of the individual components while establishing a clear interfacial interaction as evidenced by the Raman peak shifts. This structural integrity is a key factor in ensuring the stability of the active material during prolonged electrochemical cycling.

3.3 Electrochemical properties

3.3.1 Interfacial electron-transfer dynamics

The electrochemical kinetics and charge-storage mechanisms of the synthesized electrodes are systematically evaluated using cyclic voltammetry (CV), as illustrated in Fig. 5. Data collection for CV analysis is performed in a typical three-electrode cell environment. The potential sweep rate is incrementally adjusted between 10 and 70 mV s^{-1} (Fig. 5a-b). Aqueous 1 M LiCl is utilized as the electrolyte to benefit from the high mobility and small hydrated radius of Li^+ ions, which are essential for rapid charge–discharge kinetics in hierarchical heterostructures. A potential range of − 1.1 V to 0.1 V is utilized for both the WS_2/SS and CuO@WS_2/SS electrodes (Fig. 5a-c). This specific window is identified to ensure the reversible redox activity of the hybrid structures while simultaneously maintaining the electrochemical stability of the aqueous electrolyte. The CV curves exhibit well-defined redox peaks, indicating a combination of Faradaic pseudocapacitance and electric double-layer capacitance (Fig. 5a-b). Notably, the CuO@WS_2/SS electrode demonstrates significantly higher current densities compared to the pristine WS_2/SS at a constant scan rate of 70 mV s^{-1} (Fig. 5c), suggesting that the integration of CuO enhances the electroactive surface

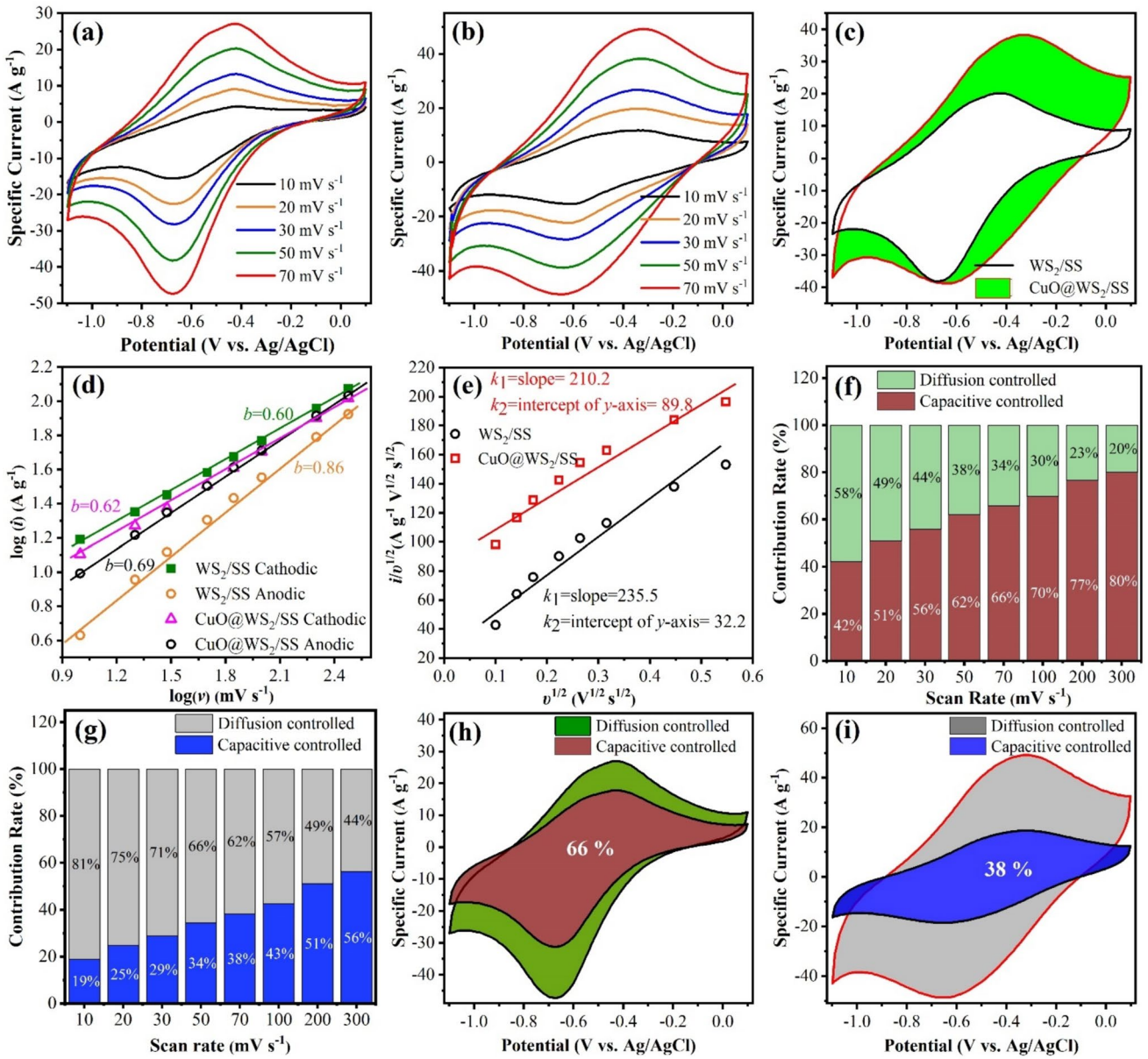


Fig. 5 Electrochemical characterization: **a** CV profiles of WS_2/SS and **b** CuO@WS_2/SS electrodes across various scan speeds. **c** Comparative CV analysis of both electrodes at a scan rate of 70 mV s^{-1}. **d** Evaluation of the b-value derived from the correlation between peak current response and scan rate. **e** Plot of $i/v^{1/2}$ versus $v^{1/2}$ for kinetic analysis. Deconvolution of capacitive and diffusion-limited contributions at 70 mV s^{-1} for **f** WS_2/SS and **g** CuO@WS_2/SS. Quantitative distribution of energy storage mechanisms for **h** WS_2/SS and **i** CuO@WS_2/SS

area and promotes faster ion diffusion. The correlation between the maxima of the current (i) and the potential sweep rate (v) is modeled using a power-law approach ($i = av^b$) to probe the kinetic nature of the process [21]. Based on the data in Fig. 5d, the b-coefficients extracted for the oxidation and reduction signals of CuO@WS_2/SS (0.60 and 0.62) and WS_2/SS (0.86 and 0.69) are situated within the 0.5–1.0 interval. These values confirm that the charge accumulation is governed by a dual-mode kinetic regime, where Faradaic diffusion and non-Faradaic surface capacitive effects coexist.

The quantitative differentiation of these contributions is performed by plotting $i/v^{1/2}$ against $v^{1/2}$

(Fig. 5e). At a scan rate of 70 mV s^{-1}, the capacitive contribution is determined to be 66% for the CuO@WS_2/SS electrode (Fig. 5h) and 38% for the WS_2/SS electrode (Fig. 5i). This marked increase in the capacitive component for the composite electrode highlights the synergistic effect of CuO and WS_2, which facilitates more efficient surface charge transfer. Furthermore, as the scan rate increases from 10 to 300 mV s^{-1}, the surface-controlled contribution becomes progressively dominant for both CuO@WS_2/SS (Fig. 5f) and WS_2/SS (Fig. 5g), reaching 80% and 56%, respectively, at the highest scan rate. These results collectively demonstrate that the CuO-decorated WS_2 heterostructure significantly optimizes rate capability and energy storage efficiency by minimizing diffusion resistance and enhancing pseudocapacitive interactions.

Based on the CV measurements, the specific capacitance for each electrode is calculated using the following equation [22]:

$$C_m = \frac{1}{m \cdot v \cdot \Delta V} \int I \cdot \Delta \mathrm{d}V \quad (1)$$

Gravimetric capacitance (C_m) is calculated based on the enclosed area of the CV profile ($\int I\, \mathrm{d}V$), where m represents the mass of the active material, I corresponds to the measured current response, and v represents the scan rate. For the bare WS_2/SS electrode, the calculated C_m values are 385.9, 306.6, 272.2, 239.1, 219.1, 203.6, 174.9, and 159.0 F g^{-1} at scan rates of 10, 20, 30, 50, 70, 100, 200, and 300 mV s^{-1}, respectively. By comparison, the CuO@WS_2/SS hybrid electrode exhibits markedly enhanced charge-storage behavior throughout the same scan-rate range, delivering C_m values of 665.5, 538.6, 477.0, 406.8, 371.4, 330.3, 265.8, and 232.5 F g^{-1}, respectively. The superior electrochemical performance of the CuO@WS_2/SS electrode is strongly governed by the optimized CuO mass loading (29.2 wt%), which enables a synergistic integration of abundant redox-active sites with efficient charge-transport pathways, thereby maximizing capacitance without compromising ion diffusion kinetics.

3.3.2 *Time-resolved charging studies and Nyquist plot analysis*

The electrodes' electrochemical energy storage capabilities are further evaluated through galvanostatic charge–discharge (GCD) measurements. Figure 6a and b displays the GCD curves of the pristine WS_2/SS and hybrid CuO@WS_2/SS electrodes recorded at different current densities ranging from 5 to 30 A g^{-1}. Both electrodes display nearly symmetric triangular charge–discharge profiles with slight deviations from linearity, indicating the presence of Faradaic pseudocapacitive behavior. Notably, the CuO@WS_2/SS electrode shows considerably prolonged discharge durations compared with the WS_2/SS electrode at all applied current densities, reflecting its enhanced charge-storage capability. Specific capacitance is calculated from the GCD data using a standard equation [23]:

$$C_s = \frac{I}{m \cdot \Delta V^2} \int V \cdot \Delta \mathrm{d}t \quad (2)$$

In this context, C_s (F g^{-1}) denotes the specific capacitance of the electrode, while I(A) corresponds to the applied current. The term $\int V\mathrm{d}t$ represents the integrated area of the discharge profile, m(g) refers to the mass of electroactive material deposited on the stainless steel substrate. Figure 6c illustrates the variation of specific capacitance obtained from GCD measurements as a function of current density. At 5 A g^{-1}, the CuO@WS_2/SS electrode exhibits a notably high specific capacitance of 527 F g^{-1}, nearly twice that of the bare WS_2/SS electrode (265 F g^{-1}). The Nyquist plots (Fig. 6d) provide insights into the internal resistance and charge-transfer kinetics. The experimental data are modeled using an equivalent circuit (inset image in Fig. 6d), and the derived parameters are summarized in Table 1. As derived from the Nyquist plots (Fig. 6d), the CuO-decorated WS_2/SS manifests a diminished solution resistance (2.11 Ω) relative to the pristine WS_2/SS sample (2.42 Ω). This lower R_s value reflects optimized interfacial contact and improved charge-transport efficiency at the electrode–electrolyte interface. The charge-transfer resistance (R_{CT}) serves as a critical indicator of the redox kinetics at the electrode–electrolyte interface. The R_{CT} value for the hybrid CuO@WS_2/SS electrode is calculated as 3.49 Ω, which represents a significant decrease compared to the WS_2/SS electrode (15.66 Ω). This dramatic drop in resistance confirms that the synergistic interaction between the CuO nanoparticles and the WS_2 matrix effectively facilitates rapid electron transfer and accelerates electrochemical reactions. Furthermore, the constant phase elements (CPE_1 and CPE_2) provide insights into the non-ideal capacitive behavior of the surface. The hybrid electrode maintains elevated CPE values (1.30 mF and 1.14

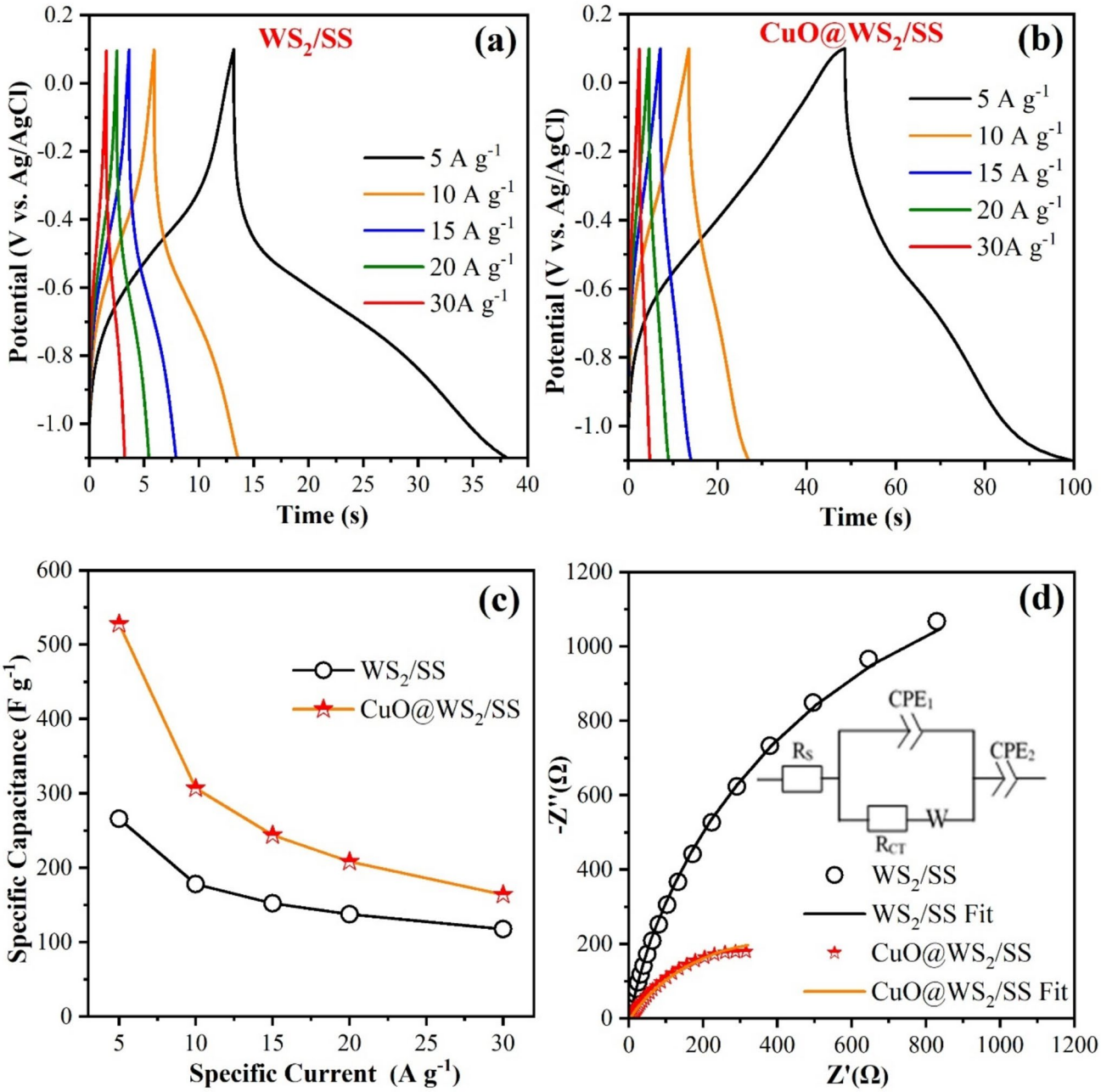


Fig. 6 Comprehensive electrochemical performance and stability analysis of the fabricated electrodes: **a–b** GCD profiles of pristine WS_2/SS and CuO@WS_2/SS at current densities ranging from 5 to 30 A g^{-1}, **c** Comparative specific capacitance as a function of specific current highlighting the performance enhancement in the hybrid structure, **d** Nyquist plots with the corresponding equivalent circuit model used for parameter extraction

Table 1 EIS parameters obtained from equivalent circuit fitting for both the electrodes and the assembled SSC device

Electrode	R_s (Ω)	R_{CT} (Ω)	CPE_1 (mF)	CPE_2 (mF)	Goodness of fit
WS_2/SS	2.42	15.66	0.87	0.06	$19.23 \cdot 10^{-3}$
CuO@WS_2/SS	2.11	3.49	1.30	1.14	$2.41 \cdot 10^{-3}$
DEVICE	2.6	12.14	11.6	5.03	$7.22 \cdot 10^{-3}$

mF) relative to the unmodified WS_2/SS (0.87 mF and 0.06 mF), reflecting an optimized electroactive surface area. The impedance analysis validates that the CuO-modified surface acts as a high-conductivity gateway, significantly lowering the interfacial energy barriers and accelerating ion flux, thereby translating into the superior kinetic efficiency observed in the hybrid electrode's performance.

3.3.3 *High-rate CuO@WS_2/SS-based symmetric prototype in LiCl electrolyte*

The symmetric supercapacitor (SSC) was fabricated using a face-to-face assembly technique to ensure optimal ionic contact and structural stability. Two identical CuO@WS_2/SS electrodes, each having an active area of 1 cm^2, were utilized as both the positive and negative terminals. To prevent electrical short-circuiting while maintaining high ionic conductivity, a porous cellulose paper was employed as the separator. The assembly began with the soaking of the cellulose separator in a 1 M LiCl aqueous electrolyte for 24 h to achieve full saturation. Subsequently, this electrolyte-impregnated separator was sandwiched between the two CuO@WS_2/SS electrodes. The entire "sandwich" architecture was then tightly sealed to ensure a robust interface between the active material and the separator, minimizing contact resistance. The resulting CuO@WS_2/SS //Cellulose// CuO@WS_2/SS configuration provides a symmetric charge distribution pathway, as schematically illustrated in Fig. 7a. The symmetric device configuration facilitates efficient ion and electron transport (Fig. 7a). The Li^+ ions from the 1 M LiCl electrolyte easily penetrate through the porous structure of the CuO@WS_2 heterostructure. The synergistic effect between the high-capacity CuO and the highly conductive WS_2 layers ensures rapid charge transfer, as visualized by the seamless interface between the active material and the SS current collector (Fig. 7a). The specific capacitance of the symmetric supercapacitor device is determined from the CV and GCD profiles according to the equations below [23]:

$$C_m = \frac{\int I dv}{Mv\Delta V} \tag{3}$$

$$C_s = \frac{2E}{M\Delta V^2} \tag{4}$$

Here, C_m (F g^{-1}) and C_s (F g^{-1}) denote the gravimetric capacitance of the full-cell assembly obtained from the CV and GCD measurements, respectively; M (g) represents the combined active mass of both electrodes; E (J) corresponds to the discharge energy; and ΔV (V) refers to the applied potential window. The operational stability of the CuO@WS_2/SS symmetric device is initially investigated by expanding the potential window from 1.1 to 1.5 V. The CV curves maintain a quasi-rectangular profile even at the elevated 1.5 V limit (Fig. 7b), signifying a robust electrochemical window without significant electrolyte decomposition. At various scan rates (Fig. 7c), the device exhibits a consistent current response, suggesting rapid ion diffusion and excellent rate capability facilitated by the CuO@WS_2/SS heterostructure. Based on the CV measurements, the SSC device delivers specific capacitance values of 159.6, 112.9, 95.7, 85.9, 76.6, 72.1, 63.3, 52.7, and 48.5 F g^{-1} at scan rates of 5, 10, 15, 20, 25, 30, 40, 60, and 80 mV s^{-1}, respectively. The gradual decrease in capacitance with increasing scan rate arises from restricted ion access at shorter timescales. At lower scan rates, ions can interact more effectively with active sites, while the relatively high capacitance retained at elevated scan rates suggests good rate performance and efficient charge transport. The GCD profiles (Fig. 7d) display nearly symmetrical triangular shapes with minimal iR drop, even at high specific currents. This behavior confirms the high reversibility and low internal resistance of the symmetric assembly. The linear discharge characteristics further indicate that the charge-storage mechanism is governed by both fast surface redox reactions and electrical double-layer contributions. At specific currents of 1, 1.2, 1.4, 1.6, 1.8, 2, 3, and 5 A g^{-1}, the specific capacitance values are 153.9, 138.3, 125.2, 113.6, 100.0, 86.9, 65.9, and 4.6 F g^{-1}, respectively.

One of the most striking features of the SSC device is its outstanding long-term stability, retaining 94.6% of its initial capacitance after 10,000 continuous cycles (Fig. 7e). This exceptional durability can be attributed to the structural synergy between WS_2 and CuO, which accommodates volume changes during ion intercalation. The Nyquist response of the SSC device is analyzed using the same equivalent circuit model applied to fit the three-electrode measurements (inset of Fig. 6d). The extracted parameters are R_s = 2.6 Ω, R_{CT} = 12.14 Ω, CPE_1 = 11.6 mF, and CPE_2 = 5.05 mF (Table 1). The relatively low series resistance suggests good overall conductivity within the device, while the

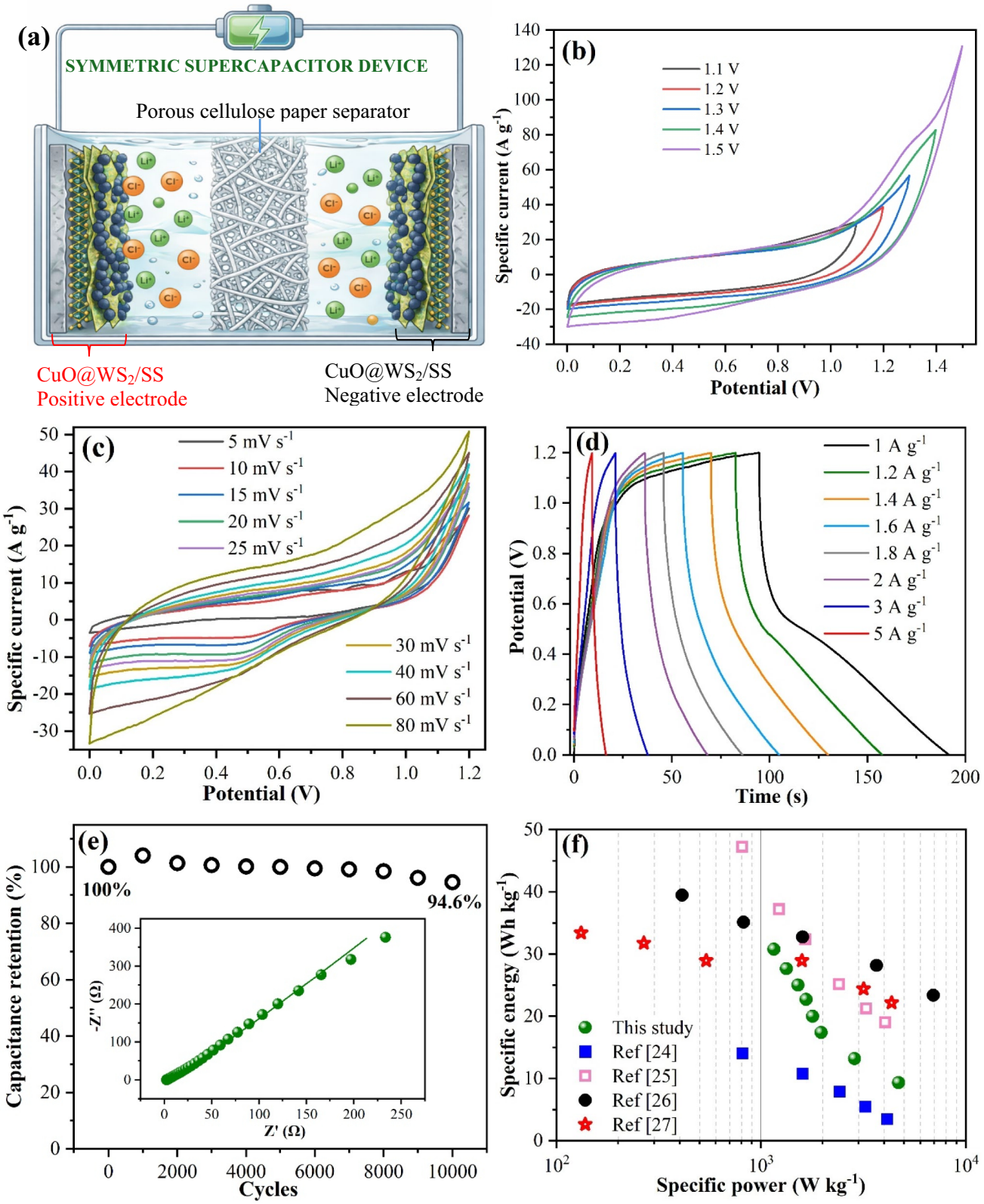


Fig. 7 **a** Schematic illustration of the assembled SSC device. **b** CV curves at different potential windows, **c** CV profiles at varying scan rates, **d** GCD curves at various specific currents, **e** Long-term cycling stability and EIS Nyquist plot (inset), **f** Ragone plot comparing the specific energy and power with literature

moderate charge-transfer resistance indicates a reasonably efficient interfacial process. The presence of two constant phase elements reflects non-ideal capacitive behavior, likely arising from surface heterogeneity and the porous electrode architecture. These parameters indicate a system with balanced charge transport and ion accessibility, while some resistive limitations remain at the electrode–electrolyte interface.

The Ragone plot (Fig. 7f) contextualizes the performance of our CuO@WS_2/SS device against previously reported studies. The device occupies a superior position in the energy-power map, delivering high energy density while maintaining substantial power output. This performance profile highlights the practical viability of using CuO@WS_2/SS architectures for high-performance, long-lasting energy storage solutions. The SSC device exhibits power densities of 1155.5, 1329.9, 1517.1, 1659.5, 1786.7, 1968.9, 2859.1, and 4696.5 W kg^{-1} at current densities of 1, 1.2, 1.4, 1.6, 1.8, 2, 3, and 5 A g^{-1}, corresponding to energy densities of 30.8, 27.7, 25.1, 22.7, 20.0, 17.4, 13.2, and 9.3 Wh kg^{-1}, respectively. This trend reflects the typical trade-off between energy and power: as the device is operated at higher power output, the accessible energy decreases. The results indicate that the SSC can maintain relatively high energy at moderate power levels, while still delivering strong power performance at lower energy densities. This balance suggests that the device is capable of operating efficiently across a wide range of conditions, with rapid charge–discharge capability becoming more dominant at higher power regimes.

To evaluate the practical viability of the materials developed herein, it is first necessary to consider the state-of-the-art results reported in recent studies [24–33], which subsequently serve as a reference for performance comparison (Table 2). Recent research by Mohan et al. [24] shows that WS_2 nanoflower electrodes with a high mass loading of 30 mg cm^{-2} deliver a specific energy of 14 Wh kg^{-1} and a power density of 800 W kg^{-1}. Their study highlights the potential of transition metal dichalcogenides (TMDs) for commercial energy storage, as the symmetric device maintains its electrochemical performance and stability throughout 10,000 continuous GCD cycles [24]. Sharma et al. [25] develop an out-of-plane CuSe/WS_2

Table 2 Comparison of WS_2-based supercapacitor electrodes reported in the literature

Electrode	Electrolyte	Specific capacitance (F g^{-1})	Specific energy (W h kg^{-1})	Specific power (W kg^{-1})	Capacitance retention	Refs.
2D WS_2 at Nifoam	6 M KOH	40 at 5 A g^{-1}	14	800	100% after 1000 cycles	[24]
CuSe/WS_2	1 M $(NH_4)_2SO_4$	555.6 at 1 A g^{-1}	48.2	800	80% after 5000 cycles	[25]
WS2-coated 3D-printed carbon electrode	polyvinyl alcohol (PVA)/Li_2SO_4 gel electrolyte	19.9 at 3.32 A g^{-1}	7.17	250	98% after 40,000 cycles	[26]
WS_2-polyanilin	6 M LiCl	6339 at 0.03 A g^{-1}	830	37,350	97.7% after 10,000 cycles	[27]
WS_2@Ni–Co–S	6 M KOH	1920.3 at 1 A g^{-1}	40	417.5	93.8% after 18,000 cycles	[28]
MOF@WS_2	1 M KOH	746 at 2 A g^{-1}	80.1	1800	83.8% after12,000 cycles	[29]
ZnO/WS_2	2 M KOH	180 at 0.5 A g^{-1}	–	–	75% after 5000 cycles	[30]
Ir-doped WS_2	1 M Na_2SO_4	568.5 at 0.5 A g^{-1}	78.5	999	88.0% after 3000 cycles	[31]
MoS_2:WS_2/CF	KOH-PVA	1097 at 1 mV s^{-1}	62.3	1300	88.7% after 5000 cycles	[32]
$SmCoO_3$:WS/NF	1 M KOH	1197 at 1 A g^{-1}	12.6	699.8	92.8% after 5000 cycles	[33]
CuO@WS_2/SS	1 M LiCl	153.9 at 1 A g^{-1}	30.8	1155.5	94.6% after 10,000 cycles	This study

heterostructure array specifically for ammonium-ion supercapacitors operating in extreme temperatures. The electrode achieves a specific capacity of 555.6 F g^{-1} at 1 A g^{-1} and delivers a high specific energy of 48.2 Wh kg^{-1} and a corresponding specific power of 800 W kg^{-1} [25]. Yang et al. [26] report the engineering of a hybrid energy storage system featuring a core–shell WS_2@Ni–Co–S architecture paired with activated carbon obtained from rose flower biomass. This heterostructure design optimizes the interface between the WS_2 core and the multi-component sulfide shell, providing an abundant network of electroactive sites that achieves a specific capacitance of 1920.3 F g^{-1} at 1 A g^{-1}. The integrated asymmetric assembly exhibits superior performance metrics, including a specific energy of 40 Wh kg^{-1} and a specific power of 417.5 W kg^{-1}. Additionally, the electrode maintains 93% of its original capacity over 18,000 cycles, proving that the combination of transition metal dichalcogenides and biomass-derived materials significantly enhances long-term electrochemical durability and energy density. Nishtha et al. [27] fabricate a WS_2/WO_{3-x} composite electrode using an atmospheric-pressure chemical vapor deposition technique. A symmetric supercapacitor device is constructed by depositing the WS_2/WO_{3-x} material onto carbon cloth [27]. The assembled device exhibits a specific capacitance of 380.8 F g^{-1} at 0.083 A g^{-1}, along with an energy density of 33.8 Wh kg^{-1} and a power density of 133.3 W kg^{-1} [27]. Furthermore, the electrode maintains nearly 84% of its initial capacitance after 2100 charge–discharge cycles at a current density of 2.6 A g^{-1} [27]. Mappoli et al. [28] introduce a novel design for energy storage by merging 3D-printing technology with transition metal dichalcogenides to create a self-supporting WS_2-carbon supercapacitor. By employing an additive manufacturing strategy, the researchers develop a three-dimensional carbon architecture integrated with a solid-state electrolyte, which delivers a specific capacitance of 19.9 F g^{-1} at a current density of 3.32 A g^{-1}. The device exhibits a promising energy output, achieving a specific energy of 7.17 Wh kg^{-1} alongside a specific power of 250 W kg^{-1} [28]. Siahboomi et al. [29] introduce an innovative light-responsive energy storage system using WS_2-polyaniline (PANI) photoelectrodes fabricated through electropolymerization. The study highlights a "photo-assisted" charging mechanism where the WS_2-PANI composite achieves a high specific capacitance of 1.5 F g^{-1} [29]. The integrated device delivers a specific energy of 830 Wh kg^{-1} and a specific power of 37,350 W kg^{-1} [29]. Furthermore, the system exhibits excellent durability by maintaining 97.7% of its initial capacity over 10,000 cycles. Ali et al. [30] investigate the multifunctional performance of a hybrid Co-MOF@WS_2 composite designed for both supercapacitor applications and the hydrogen evolution reaction (HER). By integrating cobalt-based metal–organic frameworks (Co-MOF) with WS_2 nanostructures, the researchers create a synergistic architecture that facilitates efficient charge transfer and enhances surface reactivity [30]. The composite electrode achieves a high specific capacitance of 2901 C g^{-1} at a current density of 2 A g^{-1} (or ~ 746 F g^{-1}) [30]. Furthermore, the device exhibits a specific energy of 80.1 Wh kg^{-1} and a specific power of 1800 W kg^{-1}. The material also maintains 83.8% of its initial capacity after 12,000 cycles [30]. Pant et al. [31] report a multifunctional ZnO/WS_2 composite synthesized via a hydrothermal route. The heterostructure delivers a specific capacitance of 180 F g^{-1} at 0.5 A g^{-1} and exhibits 75% stability after 5000 cycles. Siva et al. [32] explore the impact of Iridium (Ir) doping on the electrochemical properties of 1 T-phase WS_2 for symmetric supercapacitor electrodes. The study demonstrates that incorporating Ir into the 1 T-WS_2 lattice significantly enhances metallic conductivity and facilitates faster ion diffusion [32]. The optimized Ir-doped electrode delivers a high specific capacitance of 568.5 F g^{-1} at 0.5 A g^{-1} [32]. Furthermore, the symmetric device achieves a specific energy of 78.5 Wh kg^{-1}, a specific power of 999 W kg^{-1} and maintains 100% of its initial capacity over 1000 cycles [32]. Yağci et al. [33] investigate the performance of co-doped molybdenum and tungsten dichalcogenides (MoS_2:WS_2) synthesized directly on carbon felt (CF) substrates via a hydrothermal route. The study focuses on the synergistic interaction between the two transition metal dichalcogenides, which optimizes the surface architecture for enhanced charge storage [33]. The composite electrode achieves a specific capacitance of 1097 F g^{-1} at a scan rate of 1 mV s^{-1} [33]. The specific energy and specific of the MoS_2:WS_2/CF device are reported to be 62.3 Wh kg^{-1} and 1300 W kg^{-1}, respectively [33]. Furthermore, the device demonstrates high cyclic stability, maintaining 88.7% of its capacity over 5000 charge–discharge cycles [33]. The comparative analysis reveals that the CuO@WS_2/SS configuration presented in this research significantly outperforms many contemporary tungsten-based systems in terms of its integrated electrochemical profile [33]. By reaching a specific energy of 105.5 Wh kg^{-1} and a power

density exceeding 5351.3 W kg^{-1}, this heterostructure effectively bridges the gap between high-capacity battery-like behavior and high-rate supercapacitive performance. Furthermore, the 95% cycle stability demonstrates that the material design overcomes the typical degradation challenges seen in other sulfide-based composites, establishing a new performance benchmark for durable, high-energy–density hybrid supercapacitors [33]. Koventgan et al. [34] fabricate an electrode by coating samarium cobalt oxide (SCO)-loaded tungsten sulfide onto a NF substrate. Based on the SCO–WS/NF electrode, the assembled supercapacitor exhibits a wide operating potential window of 1.4 V, delivering an energy density of 12.63 Wh kg^{-1} and a power density of 699.78 W kg^{-1} [34]. Moreover, the device demonstrates excellent cycling stability, retaining 92.8% of itsinitial capacitance after 5000 charge–discharge cycles [34].

4 Conclusions

This study evaluates the electrochemical energy storage performance of WS_2/SS and CuO@WS2/SS electrodes in a three-electrode configuration. Structural analyses based on XRD and Raman spectroscopy confirm the successful formation of the WS_2 framework and the effective integration of CuO within the hybrid electrode architecture. Electrochemical impedance spectroscopy reveals that the CuO@WS_2/SS electrode possesses a larger electroactive surface area than the pristine WS_2/SS electrode, along with a markedly reduced charge-transfer resistance, which supports more efficient interfacial kinetics. Electrochemical results consistently demonstrate that the CuO@WS_2/SS electrode delivers significantly higher charge-storage performance than WS_2/SS across all measurements. The specific capacitance increases from 385 F g^{-1} for WS_2/SS to 665 F g^{-1} for the hybrid electrode at 10 mV s^{-1}, and a similar enhancement is maintained under galvanostatic conditions (265 to 527 F g^{-1} at 5 A g^{-1}). EIS results reveal that the CuO@WS_2/SS electrode exhibits a larger electroactive surface area compared to the WS_2/SS electrode. Moreover, this hybrid structure significantly reduces the charge-transfer resistance, indicating a faster charge-transfer process at the electrode–electrolyte interface. For practical application, a CuO@WS_2/SS-based symmetric supercapacitor is assembled using a cellulose paper separator and a 1 M LiCl aqueous electrolyte. The device exhibits a specific capacitance of 153.9 F g^{-1} at 1 A g^{-1}, together with an energy density of 30.8 Wh kg^{-1} and a power density of 1155.5 W kg^{-1}. Long-term cycling evaluation shows that the device retains 94.6% of its initial capacitance after 10,000 GCD cycles, confirming strong electrochemical durability.

Acknowledgements

The authors would like to acknowledge the immense support received from the Research Fund of Bursa Uludağ University, project number FGA-2024-1745.

Author contributions

Hasan Emir Kırtay contributed toward formal analysis, investigation, writing—original draft, visualization. Seyit Rıza Tokgöz contributed toward formal analysis, investigation, methodology, writing—original draft. Ahmet Peksöz contributed toward writing—review & editing, supervision, conceptualization, project administration, validation.

Funding

Open access funding provided by the Scientific and Technological Research Council of Türkiye (TÜBİTAK).

Data availability

No datasets were generated or analyzed during the current study.

Declarations

Competing interests The authors declare no competing interests.

Ethical approval This study does not involve any human participants and/or animals.

Informed consent Informed consent was received from all authors.

Open Access This article is licensed under a Creative Commons Attribution 4.0 International License, which permits use, sharing, adaptation, distribution and reproduction in any medium or format, as long as you give appropriate credit to the original author(s) and the source, provide a link to the Creative Commons licence, and indicate if changes were made. The images or other third party material in this article are included in the article's Creative Commons licence, unless indicated otherwise in a credit line to the material. If material is not included in the article's Creative Commons licence and your intended use is not permitted by statutory regulation or exceeds the permitted use, you will need to obtain permission directly from the copyright holder. To view a copy of this licence, visit http://creativecommons.org/licenses/by/4.0/.

References

1. A. Das, S.D. Peu, M.S. Hossain, M.A.M. Akanda, M.M. Salah, M.M.H. Akanda, M. Rahman, B.K. Das, Metal oxide nanosheet: synthesis approaches and applications in energy storage devices (batteries, fuel cells, and supercapacitors). Nanomaterials **13**(6), 1066 (2023). https://doi.org/10.3390/nano13061066
2. Y. Ma, X. Xie, W. Yang, Z. Yu, X. Sun, Y. Zhang, X. Yang, H. Kimura, C. Hou, Z. Guo, W. Du, Recent advances in transition metal oxides with different dimensions as electrodes for high-performance supercapacitors. Adv. Compos. Hybrid Mater. **4**, 906–924 (2021). https://doi.org/10.1007/s42114-021-00358-2
3. M.Z. Iqbal, M. Alzaid, U. Abbasi, S. Alam, R. Ali, A.M. Afzal, S. Aftab, Investigation of magnetron sputtered Ni@Cu/WS_2 as an electrode material for potential supercapattery devices. Int. J. Energy Res. **46**, 7334–7347 (2022). https://doi.org/10.1002/er.7641
4. C. Koventhan, Y.C. Chung, A.Y. Lo, H.C. Weng, W.H. Hung, Development of a polyaniline/CMK-3/hydroquinone composite supercapacitor system. Mater. Chem. Phys. **207**, 127369 (2023)
5. C. Koventhan, S. Pandiyarajan, S.M. Chen, C.S. Selvan, Novel design of perovskite-structured neodymium cobalt oxide nanoparticle-embedded graphene oxide nanocomposites as efficient active materials of energy storage devices. ACS Appl. Mater. Interfaces **15**(38), 44876–44886 (2023). https://doi.org/10.1021/acsami.3c07836
6. C. Koventhan, A.Y. Lo, C.C. Chang, M.L. Tsai, Development of high-performance supercapacitor electrodes based on CeO_2/SiO_2/CMK-3 composites. Processes **13**, 1766 (2025). https://doi.org/10.3390/pr13061766
7. L. Li, J. Gao, V. Cecen, J. Fan, P. Shi, Q. Xu, Y. Min, Hierarchical WS_2@$NiCo_2O_4$ core-shell heterostructure arrays supported on carbon cloth as high-performance electrodes for symmetric flexible supercapacitors. ACS Omega **5**, 4657–4667 (2020). https://doi.org/10.1021/acsomega.9b04434
8. Y. Ma, C. Fang, B. Ding, G. Ji, J.Y. Lee, Fe-doped Mn_xO_y with hierarchical porosity as a high-performance lithium-ion battery anode. Adv. Mater. **25**, 4646–4652 (2013). https://doi.org/10.1002/adma.201301906
9. B. He, J. Huang, P. Ji, T.K.A. Hoang, M. Han, L. Li, L. Zhang, Z. Gao, J. Ma, J. Zhi, P. Chen, Al doped manganous oxide for high-performance aqueous Zn-ion batteries. J. Power Sources **554**, 232353 (2023). https://doi.org/10.1016/j.jpowsour.2022.232353
10. M.X. Lin, F. Shao, Y. Tang, H. Lin, Y. Xu, Y. Jiao, J. Chen, Layered Co doped MnO_2 with abundant oxygen defects to boost aqueous zinc-ion storage. J. Colloid Interface Sci. **611**, 662–669 (2022). https://doi.org/10.1016/j.jcis.2021.12.136
11. B. Zhang, Y. Wan, Z. Hua, K. Tang, C. Xia, Tungsten-doped $PrBaFe_2O_5$+δ double perovskite as a high-performance electrode material for symmetrical solid oxide fuel cells. ACS Appl. Energy Mater. **4**, 8401–8409 (2021). https://doi.org/10.1021/acsaem.1c01618
12. S.J. Patil, J.H. Kim, D.W. Lee, Self-assembled Ni_3S_2//$CoNi_2S_4$ nanoarrays for ultra high-performance supercapacitor. Chem. Eng. J. **322**, 498–509 (2017). https://doi.org/10.1016/j.cej.2017.03.095
13. T. Kajana, A. Pirashanthan, D. Velauthapillai, A. Yuvapragasam, S. Yohi, P. Ravirajan, M. Senthilnanthanan, Potential transition and post-transition metal sulfides as efficient electrodes for energy storage applications: review. RSC Adv. **12**, 18041–18062 (2022). https://doi.org/10.1039/d2ra01574a
14. Q. Pan, Z. Tong, Y. Su, S. Qin, Y. Tang, Energy storage mechanism, challenge and design strategies of metal sulfides for rechargeable sodium/potassium-ion batteries. Adv. Funct. Mater. **31**(37), 2103912 (2021). https://doi.org/10.1002/adfm.202103912
15. S. Pervez, M.Z. Iqbal, Evaluation of battery-grade alkaline earth metal sulfide electrodes for energy storage applications. Int. J. Energy Res. **46**, 8093–8101 (2022). https://doi.org/10.1002/er.7712
16. Y. Sood, P.E. Lokhande, V. Kadam, C. Jagtap, H. Mudila, U. Rednam, D. Kumar, S. Ansar, Y.A. Kumar, R. Aepuru, A. Kumar, Nanocomposites combining 2D WS_2 and 1D polyaniline for enhanced high-performance

supercapacitors. J. Alloys Compd. **1005**, 176006 (2024). https://doi.org/10.1016/j.jallcom.2024.176006

17. J. Xu, C. Liu, L. Fu, Q. Liu, S. Ramakrishna, W. Tang, Room temperature ammonia sensor with high selectivity based on the composite materials assembled by CuO nanosheets and WS_2 nanoflakes. Ceram. Int. **50**, 11844–11854 (2024). https://doi.org/10.1016/j.ceramint.2024.01.088
18. C. Zhao, P. Wang, G. Niu, D. Luo, Q. Wang, F. Wang, Rapid and efficient detection of NH_3 at room temperature using CuO/WS_2 nanohybrids. IEEE Sens. J. **22**(13), 12539–12546 (2022)
19. M. Viršek, A. Jesih, I. Milošević, M. Damnjanović, M. Remškar, Raman scattering of the MoS_2 and WS_2 single nanotubes. Surf. Sci. **601**, 2868–2872 (2007). https://doi.org/10.1016/j.susc.2006.12.050
20. J. Kim, T. Begildayeva, J. Theerthagiri, C.J. Moon, A. Min, S.J. Lee, G.A. Kim, M.Y. Choi, Manifolding active sites and in situ/operando electrochemical-Raman spectroscopic studies of single-metal nanoparticle-decorated CuO nanorods in furfural biomass valorization to H_2 and 2-furoic acid. J. Energy Chem. **84**, 56–61 (2023). https://doi.org/10.1016/j.jechem.2023.05.042
21. M. Arslan Çarpan, S.R. Tokgöz, S. Düzyer Gebizli, A. Peksöz, Synthesis and properties of carbon black (CB)-added polyacrylonitrile (PAN)/nickel foam (NF) flexible electrodes by electrospinning, and their supercapacitive performance. J. Mater. Sci. Mater. Electron. **36**, 377 (2025). https://doi.org/10.1007/s10854-025-14403-z
22. A. Peksoz, H. Killi, S.R. Tokgoz, M. Arslan Carpan, Electrochemically fabrication of a composite electrode based on tungsten oxide and cobalt on 3D Ni foam for high and stable electrochemical energy storage. Mater. Today Commun. **33**, 104263 (2022). https://doi.org/10.1016/j.mtcomm.2022.104263
23. H. Torun, S.R. Tokgöz, M. Arslan Çarpan, M.H. Somay, A. Peksöz, Fabrication of a high-performance symmetrical supercapacitor based on electrochemically interconnected Cu:NiO@rGO:PANI/NF electrodes. J Energy Storage **88**, 111462 (2024). https://doi.org/10.1016/j.est.2024.111462
24. V.V. Mohan, M. Mohan, R.B. Rakhi, High performance supercapacitors based on WS_2 nanoflower electrodes with commercial-level mass-loading. Surf. Interfaces **43**, 103496 (2023). https://doi.org/10.1016/j.surfin.2023.103496
25. M. Sharma, S.P. Singh, P. Deb, Out-of-plane CuSe/WS_2 heterostructure array as a high-performance electrode material in ammonium ion supercapacitor in harsh environment of extreme temperature. Adv. Funct. Mater. **35**, 2424005 (2025). https://doi.org/10.1002/adfm.202424005
26. F. Yang, H. Guo, J. Zhang, N. Wu, M. Yang, Y. Chen, T. Zhang, L. Sun, W. Yang, Core–shell structured WS_2@Ni-Co-S composite and activated carbon derived from rose flowers as high-efficiency hybrid supercapacitor electrodes. J Energy Storage **54**, 105234 (2022). https://doi.org/10.1016/j.est.2022.105234
27. S. Nishtha, P.V. Sada, A.K. Mishra, Synthesis and electrochemical evaluation of WS_2/WO_{3-x} heterostructure for binder-free high-performance supercapacitors. Mater. Sci. Eng. B Adv. Funct. Solid-State Mater. **327**, 119256 (2026). https://doi.org/10.1016/j.mseb.2026.119256
28. S. Mappoli, K. Ghosh, M. Pumera, Integrated free-standing WS_2 3D-printed carbon supercapacitor with solid state electrolyte. Virtual Phys. Prototyp. **19**(1), e2326897 (2024). https://doi.org/10.1080/17452759.2024.2326897
29. A.S.H. Siahboomi, M.M. Momeni, H.M. Aydisheh, F. Zhang, New photo-assisted charging supercapacitors using WS_2-polyaniline photoelectrodes produced by the electropolymerization method. J. Power. Sources **666**, 239196 (2026). https://doi.org/10.1016/j.jpowsour.2025.239196
30. Q.M. Ali, R.A. Malik, M.W. Iqbal, H. Alrobei, High-performance Co-MOF@WS_2 electrode for enhanced supercapacitor efficiency and hydrogen evolution reaction. J. Mater. Sci. Mater. Electron. **36**, 963 (2025). https://doi.org/10.1007/s10854-025-15022-4
31. B. Pant, E. Munkhtur, G.P. Ojha, J. Acharya, S.T. Hong, M. Park, Hydrothermally synthesized ZnO/WS_2 composite with impressive photocatalytic, antibacterial, and electrochemical performances. Inorg. Chem. Commun. **166**, 112630 (2024). https://doi.org/10.1016/j.inoche.2024.112630
32. P. Siva, C. Sreelakshmi, T. Ravinder, M. Ghanashyam Krishna, S.V.S. Nageswara Rao, K. Vasu, Ir-doped 1T-WS_2 high performance symmetric supercapacitor electrode. J. Energy Storage **147**, 120130 (2026). https://doi.org/10.1016/j.est.2025.120130
33. Ö. Yağci, M. Beşir Arvas, S. Yazar, Synthesis of co-doped metal dichalcogenides (MoS_2:WS_2) on carbon felt electrode by hydrothermal method and supercapacitor application. Mater. Chem. Phys. **332**, 130223 (2025). https://doi.org/10.1016/j.matchemphys.2024.130223
34. C. Koventhan, S. Pandiyarajan, S.M. Chen, Perovskite-type samarium cobalt oxide adorned hexagonal tungsten sulphide nanocomposites as a high-performance electrode material for symmetric supercapacitors. J. Energy Storage **72**, 108171 (2023). https://doi.org/10.1016/j.est.2023.108171

Publisher's Note Springer Nature remains neutral with regard to jurisdictional claims in published maps and institutional affiliations.